

# Holographic tomography with scanning of illumination: space-domain reconstruction for spatially invariant accuracy

JULIANNA KOSTENCKA,<sup>1,\*</sup> TOMASZ KOZACKI,<sup>1</sup> ARKADIUSZ KUŚ,<sup>1</sup> BJÖRN KEMPER,<sup>2</sup> AND MAŁGORZATA KUJAWIŃSKA<sup>1</sup>

<sup>1</sup>Photonics Engineering Division, Institute of Micromechanics and Photonics, Faculty of Mechatronics, Warsaw University of Technology, A. Boboli 8 Street, 02-525 Warsaw, Poland

<sup>2</sup>Biomedical Technology Center of the Medical Faculty, University of Muenster, Mendelstr 17, D-48149 Muenster, Germany

\*j.kostencka@mchtr.pw.edu.pl

**Abstract:** The paper presents two novel, space-domain reconstruction algorithms for holographic tomography utilizing scanning of illumination and a fixed detector that is highly suitable for imaging of living biomedical specimens. The first proposed algorithm is an adaptation of the filtered backpropagation to the scanning illumination tomography. Its space-domain implementation enables avoiding the error-prone interpolation in the Fourier domain, which is a significant problem of the state-of-the-art tomographic algorithm. The second proposed algorithm is a modified version of the former, which ensures the spatially invariant reconstruction accuracy. The utility of the proposed algorithms is demonstrated with numerical simulations and experimental measurement of a cancer cell.

© 2016 Optical Society of America

**OCIS codes:** (170.6960) Tomography; (090.1995) Digital holography; (170.6900) Three-dimensional microscopy; (260.1960) Diffraction theory; (170.1530) Cell analysis.

## References and links

1. Y. Sung, W. Choi, C. Fang-Yen, K. Badizadegan, R. R. Dasari, and M. S. Feld, "Optical diffraction tomography for high resolution live cell imaging," *Opt. Express* **17**(1), 266–277 (2009).
2. F. Charrière, N. Pavillon, T. Colomb, C. Depeursinge, T. J. Heger, E. A. D. Mitchell, P. Marquet, and B. Rappaz, "Living specimen tomography by digital holographic microscopy: morphometry of testate amoeba," *Opt. Express* **14**(16), 7005–7013 (2006).
3. Y. Kim, H. Shim, K. Kim, H. Park, J. H. Heo, J. Yoon, C. Choi, S. Jang, and Y. Park, "Common-path diffraction optical tomography for investigation of three-dimensional structures and dynamics of biological cells," *Opt. Express* **22**(9), 10398–10407 (2014).
4. K. Kim, Z. Yaqoob, K. Lee, J. W. Kang, Y. Choi, P. Hosseini, P. T. C. So, and Y. Park, "Diffraction optical tomography using a quantitative phase imaging unit," *Opt. Lett.* **39**(24), 6935–6938 (2014).
5. A. Kuś, M. Dudek, B. Kemper, M. Kujawińska, and A. Vollmer, "Tomographic phase microscopy of living three-dimensional cell cultures," *J. Biomed. Opt.* **19**(4), 046009 (2014).
6. M. Habaza, B. Gilboa, Y. Roichman, and N. T. Shaked, "Tomographic phase microscopy with 180° rotation of live cells in suspension by holographic optical tweezers," *Opt. Lett.* **40**(8), 1881–1884 (2015).
7. J. Kostencka, T. Kozacki, A. Kuś, and M. Kujawińska, "Accurate approach to capillary-supported optical diffraction tomography," *Opt. Express* **23**(6), 7908–7923 (2015).
8. J. Kostencka, T. Kozacki, M. Dudek, and M. Kujawińska, "Noise suppressed optical diffraction tomography with autofocus correction," *Opt. Express* **22**(5), 5731–5745 (2014).
9. W. Górski and W. Osten, "Tomographic imaging of photonic crystal fibers," *Opt. Lett.* **32**(14), 1977–1979 (2007).
10. M. Dudek, M. Kujawińska, V. Parat, G. Baethge, A. Michalska, B. Dahmani, and H. Ottevaere, "Tomographic and numerical studies of polymer bridges between two optical fibers for telecommunication applications," *Opt. Eng.* **53**(1), 016113 (2014).
11. S. S. Kou and C. J. R. Sheppard, "Image formation in holographic tomography," *Opt. Lett.* **33**(20), 2362–2364 (2008).
12. E. Y. Sidky, C.-M. Kao, and X. Pan, "Accurate image reconstruction from few-views and limited-angle data in divergent-beam CT," *J. Opt. Soc. Am.* **25**, 1772–1782 (2009).
13. J. Lim, K. Lee, K. H. Jin, S. Shin, S. Lee, Y. Park, and J. C. Ye, "Comparative study of iterative reconstruction algorithms for missing cone problems in optical diffraction tomography," *Opt. Express* **23**(13), 16933–16948 (2015).

14. W. Krauze, P. Makowski, M. Kujawińska, and A. Kuś, "Generalized total variation iterative constraint strategy in limited angle optical diffraction tomography," *Opt. Express* **24**(5), 4924–4936 (2016).
15. Nanolive, "The 3D Cell Explorer" (2016), retrieved <http://nanolive.ch/>.
16. Tomocube, "3D Holographic Microscopy" (2016), retrieved <http://tomocube.com>.
17. S. Pan and A. Kak, "A computational study of reconstruction algorithms for diffraction tomography: Interpolation versus filtered-backpropagation," *IEEE Trans. Acoust. Speech Signal Process.* **31**(5), 1262–1275 (1983).
18. A. J. Devaney, "A filtered backpropagation algorithm for diffraction tomography," *Ultrason. Imaging* **4**(4), 336–350 (1982).
19. J. Kostencka and T. Kozacki, "Space-domain, filtered backpropagation algorithm for tomographic configuration with scanning of illumination," *Proc. SPIE* **9890M**, 9890 (2016).
20. A. J. Devaney, "Inverse-scattering theory within the Rytov approximation," *Opt. Lett.* **6**(8), 374–376 (1981).
21. J. Kostencka and T. Kozacki, "Computational and experimental study on accuracy of off-axis reconstructions in optical diffraction tomography," *Opt. Eng.* **54**(2), 024107 (2015).
22. A. J. Devaney, H. J. Liff, and S. Apsell, "Spectral representations for free space propagation of complex phase perturbations of optical fields," *Opt. Commun.* **15**(1), 1–5 (1975).
23. A. Kuś, W. Krauze, and M. Kujawinska, "Active limited-angle tomographic phase microscope," *J. Biomed. Opt.* **20**(11), 111216 (2015).
24. Y. Cotte, F. Toy, P. Jourdain, N. Pavillon, D. Boss, P. Magistretti, P. Marque, and C. Depeursinge, "Marker-free phase nanoscopy," *Nat. Photonics* **7**(2), 113–117 (2013).
25. E. Wolf, "Three-dimensional structure determination of semi-transparent objects from holographic data," *Opt. Commun.* **1**(4), 153–156 (1969).
26. B. Chen and J. J. Stamnes, "Validity of diffraction tomography based on the first born and the first rytov approximations," *Appl. Opt.* **37**(14), 2996–3006 (1998).
27. S. S. Kou and C. J. R. Sheppard, "Image formation in holographic tomography: high-aperture imaging conditions," *Appl. Opt.* **48**(34), H168–H175 (2009).
28. T. Kozacki, K. Falaggis, and M. Kujawińska, "Computation of diffracted fields for the case of high numerical aperture using the angular spectrum method," *Appl. Opt.* **51**(29), 7080–7088 (2012).
29. K. Falaggis, T. Kozacki, and M. Kujawinska, "Computation of highly off-axis diffracted fields using the band-limited angular spectrum method with suppressed Gibbs related artifacts," *Appl. Opt.* **52**(14), 3288–3297 (2013).
30. K.-H. Brenner and W. Singer, "Light propagation through microlenses: a new simulation method," *Appl. Opt.* **32**(26), 4984–4988 (1993).
31. B. Kemper, D. Carl, J. Schnekenburger, I. Bredebusch, M. Schäfer, W. Domschke, and G. von Bally, "Investigation of living pancreas tumor cells by digital holographic microscopy," *J. Biomed. Opt.* **11**(3), 034005 (2006).
32. M. Takeda, H. Ina, and S. Kobayashi, "Fourier-transform method of fringe-pattern analysis for computer-based topography and interferometry," *J. Opt. Soc. Am.* **72**(1), 156–160 (1982).

## 1. Introduction

Holographic-based phase tomography (HT) is a powerful, non-invasive technique, which enables quantitative characterization of transparent micro-objects by providing 3D reconstruction of refractive index distributions. The high potential of HT is widely appreciated in life sciences and biomedicine, where it is used for minimally invasive 3D imaging of unstained, living, cellular specimens [1–5]. However, to enable the study of sensitive biological materials, originally proposed HT technique applying the object rotation configuration (ORC) [2,5–10] had to be modified to minimize the risk of damaging a sample. Currently, with a few exceptions [5–7], the biomedical-oriented HT systems utilize a tomographic concept in which physical manipulation of a sample is completely eliminated. In those systems different sample projections are achieved by scanning an illumination beam, while keeping a sample and a detector fixed [1–4]. The illumination scanning configuration (ISC) is favorable in terms of noninvasivity and high speed of data acquisition. Moreover, ISC offers an advantageous 3D imaging property, i.e. increased transverse resolution [11]. However, a downside of the method is the incomplete angular range of accessible sample perspectives, which is limited by numerical aperture of an applied imaging system. The limitation leads to the so-called missing frequency problem and poor axial resolution. The problem has been already addressed, e.g. in [12,13] and with a recent two-stage strategy based on the regularization technique [14].

Regardless of its pros and cons, numerous scientific publications [1,3,4,13,14] and commercial implementations [15,16] clearly demonstrate the potential of ISC-HT for 3D

imaging in various biomedical application fields. Currently, ISC-HT systems are constantly further improved and evaluated with increasingly demanding samples such as single living cells with complex shapes or cell clusters. The growing popularity as well as the new challenges highly motivate the need for re-examination of the capabilities of the state-of-the-art ISC-HT reconstruction techniques. While most scientific works regarding ISC-HT focus mainly on the missing frequency problem, this paper primarily concerns the diffraction-related aspects. Moreover, the work investigates an important and often ignored issue of spatial variations of the reconstruction accuracy.

In ISC-HT, tomographic reconstruction is usually performed using the direct inversion algorithm (DI) [17], which is a direct implementation of the generalized projection theorem. The major disadvantage of DI is the interpolation in a 3D sample spectrum, which causes large computational errors. In ORC-HT, the error-prone spectral interpolation can be avoided by applying filtered backpropagation algorithm (ORC-FBPP) [18], which is theoretically equivalent to DI, although it is implemented in a space domain. Notably, ORC-FBPP has been developed exclusively for ORC and is not applicable for ISC [19]. This paper addresses this limitation by introducing a novel ISC-FBPP algorithm.

ISC-FBPP is one of main novelties of this work. However, the proposed algorithm, similarly to other reconstruction techniques based on the Rytov approximation [20] (e.g. ORC-FBPP, DI), suffers from spatially variant accuracy of tomographic reconstructions [21], which is caused by errors of numerical propagation realized within the Rytov approximation [22]. The mentioned effect of spatially variant accuracy was demonstrated and explained in [21] for the case of ORC-HT. In this work, we prove that the same problem affects also ISC-HT. Moreover, we propose a solution to the described problem by developing a novel tomographic algorithm, which provides spatially invariant accuracy and thus enables accurate, large-volume tomographic reconstructions. The proposed algorithm is an extension of ISC-FBPP, in which the approximated Rytov propagation is replaced with the rigorous one. The developed algorithm is referred to within this paper as extended-depth-of-focus FBPP for ISC (ISC-EDOF-FBPP). It is important to note that ISC-EDOF-FBPP is a generalization of ORC-EDOF-FBPP [21].

Both proposed tomographic reconstruction algorithms: ISC-FBPP and ISC-EDOF-FBPP are analyzed by numerical simulations and compared to the state-of-the-art reconstruction technique, i.e. DI. They are also applied to experimental measurement data from a pancreatic cancer cell that were obtained with a Mach-Zehnder digital holographic microscope utilizing a conical illumination scenario [14,23,24]. The ISC-HT setup with the applied illumination scenario is characterized in this paper by providing the analytical formulas for its tomographic transfer function, which represents an additional important novelty of this work.

The paper is organized as follows. Section 2 provides principles of ISC-HT. Section 3 describes the novel tomographic approaches, which are analyzed in Sec. 4 by numerical simulations. Section 5 presents the experimental results. Finally, Sec. 6 summarizes the findings and draws conclusions.

## 2. Basics of holographic tomography with scanning of illumination

### 2.1 Data acquisition

The ISC-HT measurement is performed using a digital holographic microscope, which enables the acquisition of optical fields that are scattered by a sample. For a tomographic measurement, multiple scattered waves are captured, each for a different perspective, which is achieved by scanning the illumination direction (Fig. 1). Therefore, a stationary sample, immersed in a medium with refractive index  $n_0$ , is successively illuminated with multiple plane waves  $U_i$  of various wave vectors  $\mathbf{k}_i = [k_{ix}, k_{iy}, k_{iz} = (n_0^2 k_0^2 - k_{ix}^2 - k_{iy}^2)^{1/2}]$ , where  $k_0 = 2\pi/\lambda$  and  $\lambda$  is the light wavelength. The reconstructed set of scattered waves  $U_s$  is then processed with a tomographic algorithm, which recovers the 3D refractive index distribution  $n(x,y,z)$ .

The applied set of illumination directions may be specific for different ISC-HT systems. However, in all configurations, the illumination directions have to be within the acceptance cones of the numerical apertures of illumination ( $NA_{ILL}$ ) and imaging ( $NA_{IMG}$ ) systems, which is a source of the missing frequency problem.

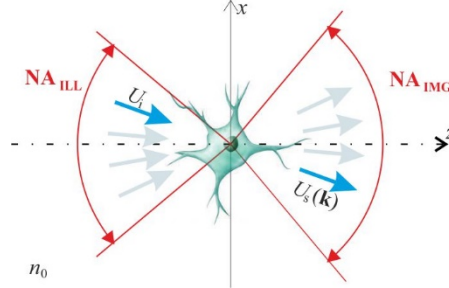


Fig. 1. A scheme of ISC-HT;  $U_i$  – illuminating plane wave,  $U_s$  – scattered wave.

### 2.2 Tomographic reconstruction with the direct inversion method

The state-of-the-art tomographic reconstruction method for ISC-HT is DI [17]. DI is a direct implementation of the generalized projection theorem, which states that a single scattered field  $U_s$  provides information about the object spatial frequency components that are located on a spherical cap, called Ewald sphere, in a 3D object spectrum [25]. This principle is valid under the first-order Born or Rytov approximation. The latter is known to be less strict in terms of the weak-scattering requirement [26]. For this reason, this work focuses solely on the Rytov solution. Within the Rytov approximation, the 3D scattering can be expressed as:

$$\tilde{\varphi}_{si}(\mathbf{k}) = n_0 k_0 / 2k_z \cdot \tilde{O}(\mathbf{k} - \mathbf{k}_i), \quad (1)$$

where  $\tilde{\cdot}$  denotes the Fourier transformation and  $\mathbf{k} = [k_x, k_y, k_z = (n_0^2 k_0^2 - k_x^2 - k_y^2)^{1/2}]$  are spatial frequency components of the Rytov scattered field:

$$\varphi_{si} = i / (k_0 n_0) \cdot \text{unwrap}[\ln(U_s / U_i)], \quad (2)$$

where ‘unwrap’ states for the phase unwrapping. In Eq. (1),  $\mathbf{K} = \mathbf{k} - \mathbf{k}_i$  is the spatial frequency vector of a scattering potential  $O$ , which is related to the refractive index distribution via:

$$O(x, y, z) = 1 - n(x, y, z)^2 / n_0^2. \quad (3)$$

Equation (1) shows that by varying the illumination direction, it is possible to cover considerably large volume of  $\tilde{O}$ , which theoretically ensures precise restoration of a sample. The outlined approach is directly adopted in DI (Fig. 2), in which a finite number of scattered waves is used for filling  $\tilde{O}$ . The filling process is realized with an interpolation method, most commonly the nearest neighbor interpolation. Afterwards,  $n(x, y, z)$  is obtained by the 3D inverse Fourier transformation of  $\tilde{O}$ .

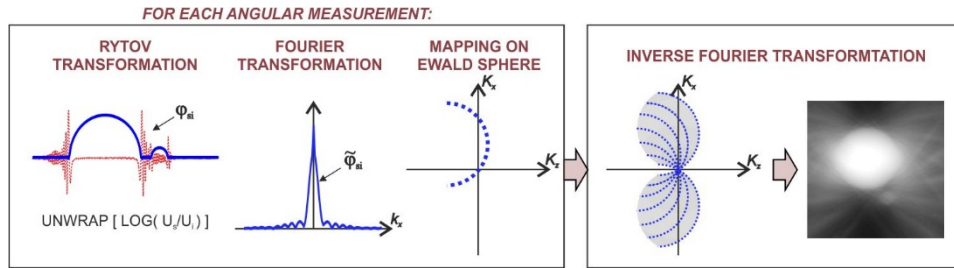


Fig. 2. Scheme of the direct inversion tomographic reconstruction algorithm for ISC-HT.

### 3. Space-domain reconstruction approach for ISC-HT

The generalized projection theorem provides an elegant solution to the problem of tomographic reconstruction. However, DI results suffer from the errors of interpolation in the Fourier domain [17]. The problem can be avoided by utilizing the concept [20] proposed by Devaney, who showed that mapping of the scattered fields onto the Ewald sphere is the Fourier-domain equivalent of propagating the data to multiple axial positions using the approximated Rytov propagation formula [22]. The concept was implemented in ORC-FBPP [18]. Additionally, in [21] it was proven that the accuracy of ORC-FBPP can be further improved by replacing the approximated Rytov propagation with the rigorous one, which yields ORC-EDOF-FBPP.

The outlined space-domain reconstruction approaches are applicable only to ORC-HT. The aim of this section is to provide the analogical solutions for ISC-HT. This is achieved by introducing two key modifications to the original ORC reconstruction techniques: 1) application of accurate and efficient methods for propagation of highly off-axis fields (Sec. 3.1); 2) development of a general solution for merging the backpropagated views, which can be applied for arbitrary illumination scenario of ISC-HT (Sec. 3.2).

#### 3.1 Backpropagation of highly off-axis fields

##### Rytov backpropagation for off-axis fields

In the case of ORC-FBPP, where the on-axis illumination is applied ( $k_{ix} = k_{iy} = 0$ ), the Rytov backpropagation process is expressed as [18]:

$$\Pi_{\text{ORC-FBPP}}^{\text{R}}(x, y; z) = \frac{e^{-i\mu_0 k_0 z}}{(2\pi)^2} \iint \tilde{\varphi}_{\text{si}}(k_x, k_y) \cdot H(k_x, k_y; z) \exp\{i(k_x x + k_y y)\} dk_x dk_y, \quad (4)$$

where the propagation kernel  $H = \exp(izk_z)$ . The key challenge in developing ISC-FBPP is an extension of Eq. (4) to the case of off-axis propagation directions. According to the Devaney's work [22], the approximated Rytov propagation approach is sufficiently accurate only if the input field can be considered as a small deviation from a plane carrier wave. In ORC-HT, a weakly scattering sample and the on-axis plane wave illumination are assumed, thus the Rytov's deviation condition is satisfied and Eq. (4) holds. In ISC-HT, the Rytov deviation condition is also satisfied, however, in this case the plane carrier wave of  $\varphi_{\text{si}}$  is highly off-axis prohibiting direct application of Eq. (4). That is because the division step ( $U_s/U_i$ ) in Eq. (2), which is evaluated before Eq. (5), erases information about the off-axis propagation direction. Notably, accounting for the off-axis carrier requires modification of the Rytov propagation formula by using the shifted spectral coordinates  $[k_x', k_y'] = [k_x - k_{ix}, k_y - k_{iy}]$ :

$$\Pi_{\text{ISC-FBPP}}^{\text{R}}(x, y; z) = \frac{e^{-i\mu_0 k_0 z}}{(2\pi)^2} \iint \tilde{\varphi}_{\text{si}}(k_x', k_y') \cdot H(k_x', k_y'; z) \exp\{i[k_x' x + k_y' y]\} dk_x' dk_y'. \quad (5)$$

The applicability issue of the standard and proposed Rytov propagation formula is illustrated in Fig. 3 for a cylindrical sample and the off-axis propagation direction tilted by  $30^\circ$  against the optical axis. The invalid use of the standard Rytov propagation [Eq. (4)] results in erroneous propagation of the field in on-axis direction (Fig. 3(a)-3(b)), while application of the formula with shifted coordinates [Eq. (5)] maintains the proper propagation direction.

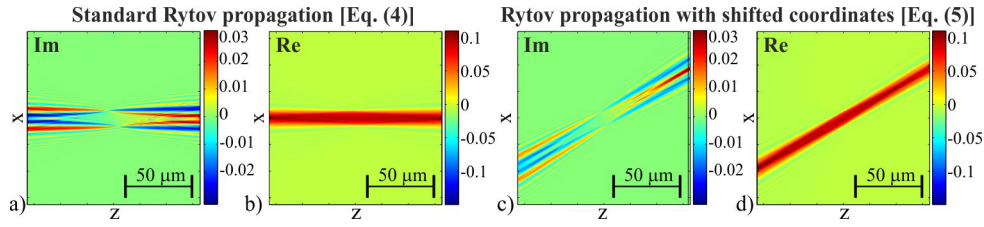


Fig. 3. The results  $\Pi_{\text{ISC-FBPP}}^{\text{R}}$  obtained using (a,b) standard and (c,d) frequency-shifted Rylov propagation formulas for a cylinder sample of diameter  $10\mu\text{m}$  and propagation direction tilted by  $30^\circ$  against the optical axis.

### Rigorous angular spectrum backpropagation for off-axis fields

The accuracy of ORC-FBPP can be significantly improved [21] by replacing the approximated Rylov propagation with the rigorous angular spectrum (AS) propagation method [28], which enables obtaining ORC-EDOF-FBPP. While in [21] the solution is provided for ORC-HT, in this paper it will be shown that the same principle holds also for ISC-HT. In ISC-EDOF-FBPP, the rigorous backpropagation process can be performed in two theoretically equivalent ways:

- 1) By propagating the original off-axis scattered wave  $U_s$  using the conventional AS [28] with non-shifted coordinates:

$$\Pi_{\text{ISC-EDOF}}(x, y, z) = \frac{e^{-in_0k_0z}}{(2\pi)^2} \iint \tilde{U}_s(k_x, k_y) \cdot H(k_x, k_y; z) \exp\{i(k_x x + k_y y)\} dk_x dk_y. \quad (6)$$

In this approach, the carrier plane wave component of  $U_s$  has to be removed after the backpropagation step by dividing by  $U_i$ .

- 2) Using the frequency-shifted AS propagation method [29], where the input field is the scattered wave with removed off-axis plane wave component  $U_{\text{si}} = U_s/U_i$ :

$$\Pi_{\text{ISC-EDOF}}(x, y, z) = \frac{e^{-in_0k_0z}}{(2\pi)^2} \iint \tilde{U}_{\text{si}}(k_x', k_y') \cdot H(k_x', k_y'; z) \exp\{i(k_x' x + k_y' y)\} dk_x' dk_y'. \quad (7)$$

In ISC-EDOF-FBPP, after the backpropagation process, the successive distributions  $\Pi_{\text{ISC-EDOF}}^{\text{R}}$  undergo the Rylov transformation:

$$\Pi_{\text{ISC-EDOF}}^{\text{R}} = i / (k_0 n_0) \cdot \text{unwrap}[\ln(\Pi_{\text{ISC-EDOF}})]. \quad (8)$$

The shifting property of Fourier transformation (FT) of an optical field:

$$\text{FT}^{-1}\{\tilde{U}_s(k_x - k_{\text{ix}}, k_y - k_{\text{iy}})\} = U_s(x, y) \exp\{-i(k_{\text{ix}}x + k_{\text{iy}}y)\} = U_{\text{si}}(x, y) \quad (9)$$

guarantees that Eqs. (6) and (7) are theoretically equivalent. However, in practice, their computation results differ significantly due to the numerical implementation issues. The off-axis backpropagation with Eq. (7) is more advantageous because the flat phase distribution of  $U_{\text{si}}$  provides favorable boundary conditions for Fast Fourier Transform, which is used in numerical implementation of Eqs. (6) and (7). Hence, the typical border errors are avoided. The effect of the border error reduction is demonstrated in Fig. 4 by a comparison of the backpropagated distributions that were obtained with standard [Eq. (6)] and the frequency-shifted [Eq. (7)] method (Fig. 4(a), 4(b) and 4(c), 4(d), respectively). The off-axis propagation with the standard method causes strong artefacts, which limit the effective reconstruction area. In this case, to separate the artefacts from the object, it is necessary to extend the computational matrix, e.g. by zeropadding, which increases the computation load. In contrast, for the frequency-shifted propagation, the obtained distribution is free of the border errors.

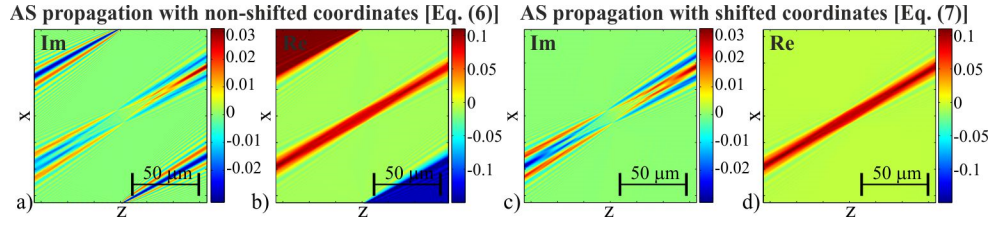


Fig. 4. The backpropagated views obtained with standard (a,b) and the frequency-shifted (c,d) propagation formula.

Note that in the case of the Rytov propagation approach, the backpropagation process can be done only using the frequency-shifted formula [Eq. (5)]. In this case, modification of Eq. (5) to non-shifted coordinates is not possible because:

$$FT^{-1}\{\tilde{\varphi}_s(k_x - k_{ix}, k_y - k_{iy})\} = \varphi_s(x, y) \exp\{-i(k_{ix}x + k_{iy}y)\} \neq \varphi_{si}(x, y), \quad (10)$$

where  $\varphi_s$  is the Rytov field without removed plane wave carrier:  $\varphi_s = i/(k_0 n_0) \ln(U_s)$ .

### 3.2 Merging of the backpropagated contributions

The second step of the elaborated space-domain tomographic algorithms is merging of the obtained backpropagated distributions  $\Pi^R$  corresponding to successive illumination directions. In ORC-FBPP, the merging process is achieved by a simple summation of all distributions  $\Pi^R$ . However, the summation of  $\Pi^R$ , which is equivalent to summation of the corresponding Ewald spheres, leads to over-representation of the sample spatial frequency components that are located in the areas of overlapping of multiple Ewald spheres. In ORC-FBPP, this problem is addressed by high-pass filtering of the scattered fields before the backpropagation [18]. However, this method is not effective [19] for ISC-HT as its geometrical conditions are completely different than for ORC-HT.

Here, to deal with the frequency over-representation problem for ISC-HT, we propose a new, more general solution, which can be used for arbitrary illumination scenario of ISC-HT. We propose to, firstly, sum all contributions  $\Pi^R$  and, then, normalize the spectrum of the initial reconstruction using a function  $c$ , which expresses the local density of Ewald spheres in the sample spectrum:

$$\tilde{O}_{\text{norm}}(\mathbf{K}) = \tilde{O}(\mathbf{K}) / c(\mathbf{K}). \quad (11)$$

The function  $c$  in Eq. (11) can be regarded as a tomographic transfer function that depends on the applied illumination scenario, the light wavelength, the refractive index of the immersion liquid and the numerical aperture of the imaging system. The flows of both reconstruction algorithms are presented in Fig. 5 (ISC-FBPP) and Fig. 6 (ISC-EDOF-FBPP).

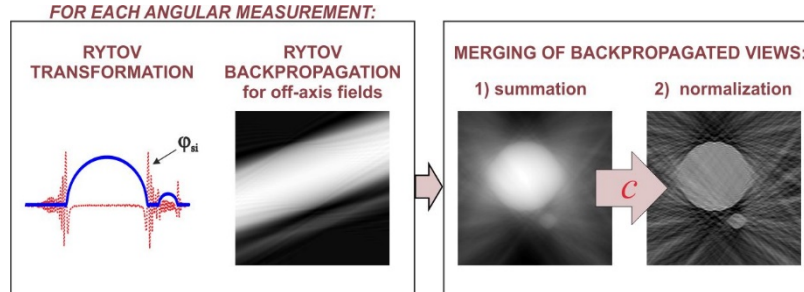


Fig. 5. Schematic illustration of the proposed ISC-FBPP.

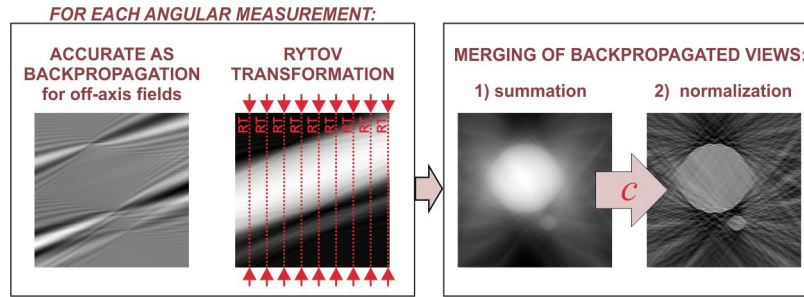


Fig. 6. Schematic illustration of the proposed ISC-EDOF-FBPP.

The key element of the proposed reconstruction algorithms is calculation of  $c$ . This can be achieved basing on the geometrical interpretation of Eq. (1), which states that  $c$  is the sum of multiple Ewald spheres. In this approach, the influence of the limited numerical aperture of the imaging system can be also considered by taking into account that the individual Ewald contributions are not full spheres but parts of the spherical caps. This geometrical approach was adapted by Kou and Sheppard [27], who provided analytical expressions for  $c$  for a linear illumination scenario, where the illumination vector is varied only in one plane containing the optical axis. Although the experimental implementation of the linear illumination scenario is relatively simple, its transfer function is highly anisotropic, which leads to strong artefacts in tomographic reconstructions. In this paper, we calculate  $c$  for another popular and more beneficial tomographic system, which applies conical illumination scenario [14,23,24] (see Appendix), where the illumination vector with a fixed inclination angle rotates around the optical axis in a full angle. The comparison of  $c$  for both illumination scenarios is presented in Fig. 7. The figure shows that the conical illumination provides larger and more symmetric frequency support than the linear one, thus it provides better 3D imaging capabilities.

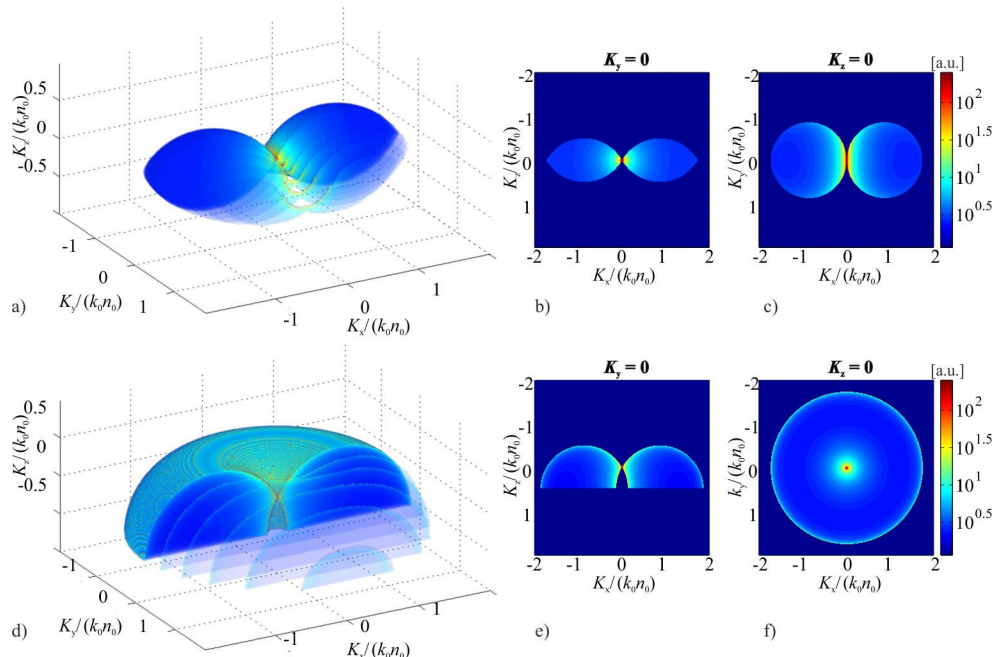


Fig. 7. a) d) 3D distributions and b-c) e-f) cross-sections of tomographic transfer functions for the ISC-HT systems with: upper row – linear illumination scenario (the illumination vector  $k_i$  rotates around  $y$ -axis in a range of  $\pm 60^\circ$ ); lower row – conical illumination scenario ( $k_i$  is inclined with respect to the optical ( $z$ ) axis by  $60^\circ$ ).



#### 4. Performance characterization by numerical simulations

The aim of this section is to test the proposed tomographic algorithms, i.e. ISC-FBPP and ISC-EDOF-FBPP (the version with frequency-shifted propagation) with numerical simulations, and to compare the results with the state-of-the-art algorithm, i.e. DI. The test object is a cylindrical phantom of a diameter  $10\mu\text{m}$  and refractive index  $n_s = 1.01$ . The simulation investigates three sample locations  $z_s = \{-20\mu\text{m}, 0\mu\text{m}, 20\mu\text{m}\}$  with respect to the central plane of the reconstruction, which allows us to study spatial changes in the reconstruction accuracy. For simplicity, the simulation is two-dimensional and represents an ISC-HT system with the linear illumination scenario (scanning range  $\pm 60^\circ$  with a step  $1^\circ$ ). Other simulation parameters:  $n_0 = 1$ ,  $\lambda = 0.5\mu\text{m}$ . The scattered waves were obtained using the wave propagation method [30].

Note that this paper does not address the missing frequency problem, which is caused by a limited angular range of accessible illumination directions and which leads to incomplete, anisotropic support of the ISC-HT transfer function. We do not intend to fill in the missing information as it is done in [12–14]. Instead, the paper focuses on the ability of the tomographic algorithms to properly recover those object frequencies that are directly accessible to a given ISC-HT system. Therefore, in this paper, we evaluate the accuracy of the tomographic algorithms by comparing their reconstruction results to the reference refractive index distribution (Fig. 8(a)), which represents the original sample distribution, whose spectrum outside the support of  $c$  is set to zero. We refer to this distribution as the ideal reconstruction.

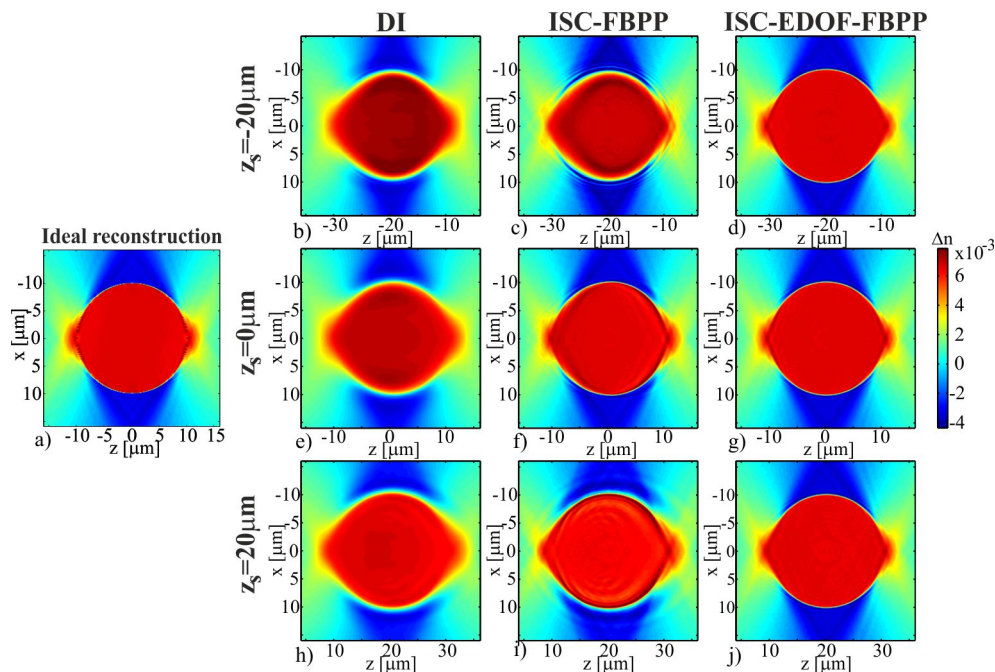


Fig. 8. (a) Ideal reconstruction; (b-j) tomographic reconstructions of a cylindrical sample.

The refractive index distributions that were recovered with the considered tomographic algorithms are presented in Fig. 8(b)–8(j) (the images show only small regions of the obtained reconstructions located around the sample). Let us first consider the reconstructions in Fig. 8(e)–8(g), which correspond to  $z_s = 0$  when the sample is located at the central slice of the reconstruction and the scattered fields are in-focus. The DI reconstruction (Fig. 8(e)) is intensively blurred, which is caused by the errors of interpolation in the Fourier domain. Notably, in this study, the most popular type of DI that applies the nearest neighbor

interpolation was used and with more accurate interpolation the blurring should decrease. Nonetheless, the reconstructions obtained with ISC-FBPP and ISC-EDOF-FBPP (Fig. 8(f), 8(g)) appear much sharper than the result of DI. The ISC-FBPP result is slightly distorted, while the distribution obtained with ISC-EDOF-FBPP well resembles the ideal reconstruction.

Let us now consider the case in which the sample is located far from the central plane and the scattered waves are strongly defocused (Fig. 8(b)-8(d), 8(h)-8(j)). In this case, the accuracy of DI and ISC-FBPP is significantly decreased. This is caused by the fact that the Rytov approximation does not hold for strongly defocused fields [22]. Notably, the character of the deformation for DI and ISC-FBPP is very similar, which is in accordance with the fact that both algorithms are theoretically equivalent. Interestingly, the deformation has the focusing-like nature i.e. the reconstructions are broaden/shrunk in size and decreased/increased in refractive index value for positive/negative  $z_s$ . The described effect is very disadvantageous because it hinders proper evaluation of size and refractive index value of a specimen. The adverse effect can be avoided by using ISC-EDOF-FBPP, which provides the same, high reconstruction accuracy for all three investigated sample positions. The described effect of the  $z$ -variant performance of DI and ISC-FBPP can be also observed in Fig. 9, which shows central, transverse cross-sections through the refractive index maps in Figs. 8(b), 8(e), 8(h) (Fig. 9(a)), Figs. 8(c), 8(f), 8(i) (Fig. 9(b)) and Figs. 8(d), 8(g), 8(j) (Fig. 9(c)).

To further investigate this effect, we repeated the described simulation for multiple sample locations  $z_s$ . For each  $z_s$ , we computed the root-mean-square-error:

$$RSME = \sqrt{\sum (\Delta n_{rec} - \Delta n_{ideal})^2 / N}, \quad (12)$$

where  $\Delta n_{rec}$  and  $\Delta n_{ideal}$  are the reconstructed and ideal refractive index variation and  $N$  denotes the reconstruction area in pixels.

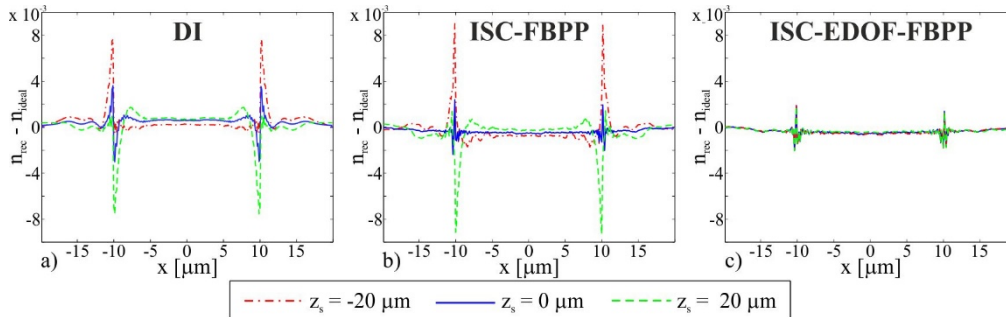


Fig. 9. Central transverse cross-sections through the refractive index difference maps in Figs. 8(b)-8(j).

The obtained results (Fig. 10) allow three conclusions:

- 1) The accuracy of DI and ISC-FBPP decreases significantly with increasing  $|z_s|$ , which is caused by invalid application of the Rytov approximation to strongly defocused fields. This prohibits accurate, large-volume tomographic reconstruction with those methods.
- 2) The reconstruction errors for DI are generally larger than for the two other methods, which is caused by inaccuracies of spectral interpolation. Note that for large negative propagation distances ( $z_s < -10 \mu\text{m}$ ), the DI error is slightly smaller than for ISC-FBPP. This is probably the result of the blurring property of DI, which to some extent compensates the focusing-like (shrinking) distortion that is related to invalid use of the Rytov approximation.

- 3) ISC-EDOF-FBPP provides the lowest reconstruction error of all investigated methods. Only for this method, the reconstruction error is  $z$ -invariant, which is achieved by introducing the rigorous propagation instead of the approximated one. Thus, ISC-EDOF-FBPP offers the highest possibility for successful restoration of large-volume objects.

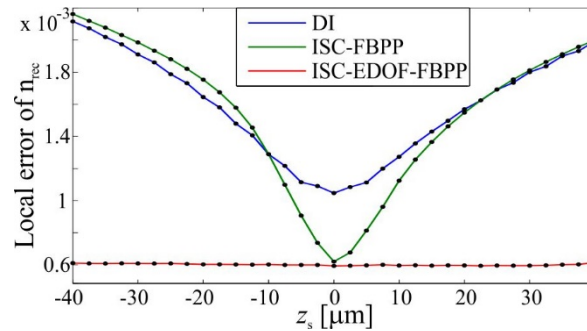


Fig. 10. The reconstruction errors for various sample locations.

The computation times of the investigated algorithm were 0.7s, 22s and 65s for DI, ISC-FBPP and ISC-EDOF-FBPP, respectively. The reconstruction parameters were: the scattered field size  $N_x = 2048$ , number of the illumination directions  $N_{\text{ill}} = 121$ , the reconstruction size  $P_x \times P_z = 2048 \times 2048$ . The computations were run in Matlab on PC with Intel® Core i7 3.40GHz and 16 GB RAM without any advanced optimization like parallel nor GPU computing. The main cause for the increased computation time of ISC-EDOF-FBPP are multiple unwrapping operations:  $N_{\text{unwrap}} = N_{\text{ill}} \times N_z$  [21] (in DI and ISC-FBPP:  $N_{\text{unwrap}} = N_{\text{ill}}$ ).

## 5. Tomographic imaging of a pancreatic cancer cell

In this section the proposed reconstruction algorithms are applied for a tomographic measurement of a pancreatic tumour cell (PaTu 8988 T pLXIN E-Cadherin [31]). For the measurements, PaTu 8988 T pLXIN E-Cadherin cells were seeded subconfluently into microscopy Petri dishes (ibidi  $\mu$ -Dish, ibidi GmbH, Munich, Germany), fixed with paraformaldehyde, covered with a glass cover slip (thickness: 170  $\mu\text{m}$ ) and observed at room temperature in phosphate buffered saline (PBS, refractive index  $n_0 = 1.337$ ). The holographic data was obtained with a scanning-mirror-based ISC-HT system with a conical illumination scenario (Fig. 11).

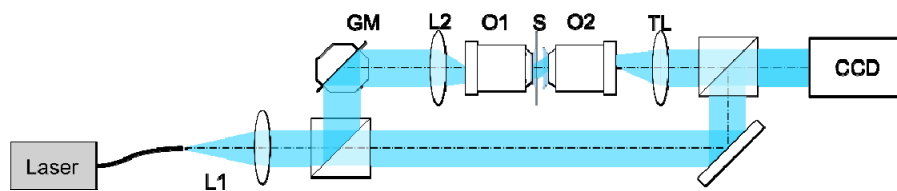


Fig. 11. The ISC-HT measurement setup. Here, the vertical setup is demonstrated horizontally.

The system consists of a collimated, coherent light source (Ti:Sapphire; 488nm), which is split into reference and object beam. The object beam is reflected off the dual-axis galvanometer mirror (GM) and focused in the front focal plane of a microscope objective (O1; 100x, NA1.3) by the L2 lens so that the measured object is illuminated by a plane wave. The sample is then imaged by an identical microscope objective (O2) and a tube lens (TL) onto a CCD camera (1/3", 2048x2456, pixel size: 3.45 $\mu\text{m}$ ), where it interferes with the reference beam generating an off-axis holograms. The conical illumination scenario applied here allowed 360 illumination directions with an angular step of 1°. The illumination directions were tilted with respect to the optical axis by an angle of 42°. For each illumination

direction, an off-axis hologram was registered and reconstructed using the Fourier Transform hologram reconstruction method [32]. During this step, the plane wave carrier components of the off-axis scattered fields were removed, giving the frequency-shifted distributions  $U_{si}$ . The data was then processed with three discussed tomographic reconstruction algorithms.

In order to provide an insight into the structure of the investigated sample, in Fig. 12, we present two transverse ( $xy$ ) cross-sections of the PaTu 8988 T pLXIN E-Cadherin cell refractive index tomogram obtained with ISC-EDOF-FBPP (Fig. 12(a) - the upper region of the cell; Fig. 12(b) - the region near to the Petri dish bottom). The outer cell borders, the nucleus, the nucleoli and vacuoles inside the cytoplasm are clearly resolved.

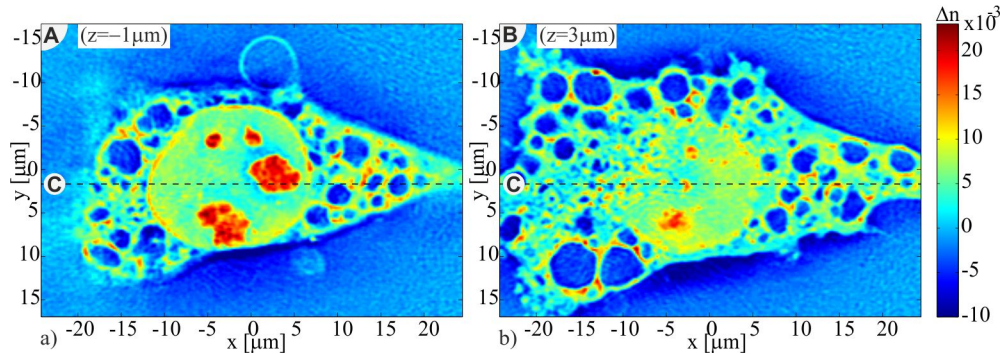


Fig. 12. Transverse cross-sections of ISC-EDOF-FBPP reconstruction of the PaTu cell (See Visualization 1).

Figure 12 demonstrates the ability of ISC-HT to produce high-resolution refractive index images in transverse cross-sections of a sample. However, the true ambition of ISC-HT is to provide high-quality axial sample images. One obstacle in achieving this goal is the missing-frequency problem, which results in poor axial resolution. However, other important yet often ignored obstacle is the  $z$ -variant accuracy of the standard reconstruction algorithms. To investigate this issue, in Fig. 13 we present axial ( $xz$ ) cross-sections of the 3D reconstructions obtained with three tomographic algorithms: DI, ISC-FPP, ISC-EDOF-FBPP. The location of the cross-sections is marked in Fig. 12 with a dashed line. The first observation is that the DI reconstruction (Fig. 13(a)) is more blurred than other results. This is presumably caused by the errors of interpolation in the Fourier domain. Secondly, ISC-EDOF-FBPP (Fig. 13(c)) indeed seems to provide improved reconstruction accuracy for non-zero axial distances. This can be observed in the marked area of the cell (a dotted ellipse), where ISC-EDOF-FBPP enables proper restoration of the cell membrane, which is not achieved with the other two algorithms.

Figure 13 proves that the  $z$ -variant accuracy of DI and ISC-FBPP can be a problem even for a relatively small sample, such as a thin biological cell. However, the shortcomings of DI and ISC-FBPP should become even more evident for larger samples or for groups of distributed samples. To demonstrate this effect, we numerically simulated the situation in which the investigated cell is located at  $z_s = \{-20\mu\text{m}, 0\mu\text{m}, 20\mu\text{m}\}$ . To achieve this, we numerically refocused the original scattered fields by  $20\mu\text{m}, 0\mu\text{m}, -20\mu\text{m}$ , respectively. For each sample location, tomographic reconstructions were performed. The obtained results are displayed in Fig. 14, in which we present a small area of the reconstructions containing the cell nucleolus.

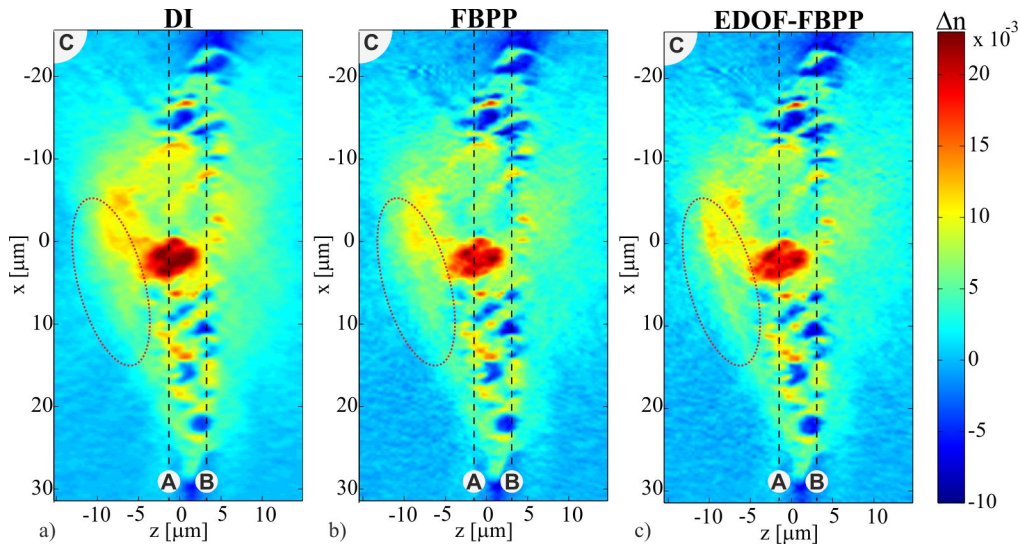


Fig. 13. Axial cross-sections of the PaTu cell reconstructions obtained with DI, ISC-FBPP, ISC-EDOF-FBPP (see Visualization 2).

The obtained images are in agreement with the simulation results (Fig. 8), i.e. the peripheral reconstructions obtained with DI and ISC-FBPP suffer from the focusing-like distortions, which lead to significant changes in size and refractive index values of the cell structure. In order to provide a quantitative comparison of the  $z$ -variant performance of the algorithms,  $RMSE$  was calculated according to Eq. (13), in which we assume that, for a given algorithm, the ideal distribution  $\Delta n_{\text{ideal}}$  is the reconstruction obtained for the central ( $z_s = 0$ ) location of the sample. The  $RMSE$  error, expressing the discrepancy between in-plane and out-of-plane reconstructions, is similarly large for DI and ISC-FBPP ( $RMSE \approx 2 \times 10^{-3}$ ), while for ISC-EDOF-FBPP, it is approx. 30 times smaller, which proves its  $z$ -invariant character.

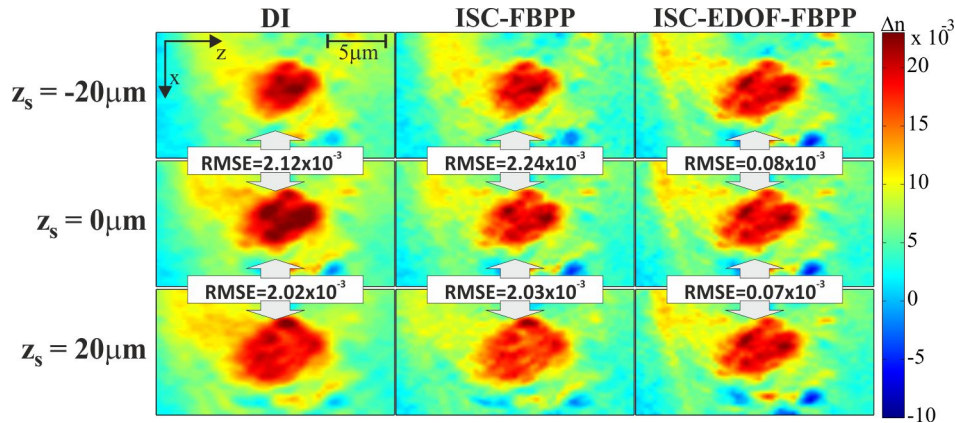


Fig. 14. Fragments of the reconstructions of a PaTu cell obtained for different sample locations ( $z_s$ ); the  $RMSE$  error denotes discrepancy between the in-plane ( $z_s = 0$ ) and out-of-plane ( $|z_s| > 0$ ) reconstructions.

The computation times of the investigated algorithm were 5min., 1.5h and 5.5h for DI, ISC-FBPP and ISC-EDOF-FBPP, respectively. The reconstruction parameters were  $N_x \times N_y = 800 \times 800$ ,  $P_x \times P_y \times P_z = 800 \times 800 \times 401$ ,  $N_{\text{ill}} = 360$ .

## 6. Conclusions

We presented two novel tomographic reconstruction algorithms for ISC-HT: ISC-FBPP and ISC-EDOF-FBPP. The developed algorithms have three major advantages:

- 1) They are implemented in the space domain, therefore, the error-prone interpolation in the object spectrum is avoided;
- 2) The algorithms are general, i.e. they can be applied for arbitrary illumination scenario;
- 3) ISC-EDOF-FBPP, unlike DI and ISC-FBPP, provides  $z$ -invariant performance, which enables maintaining high accuracy of reconstruction in a large measurement volume.

The development of the space-domain reconstruction algorithms posed two major challenges: 1) the need for accurate and efficient numerical propagation of highly off-axis fields; 2) the problem of over-representation of some spectral components in a reconstruction. Challenge 1 was approached with the specialized off-axis propagation methods utilizing shifted coordinates. Challenge 2 was addressed with a general method of the spectrum equalization using a tomographic transfer function of a given ISC-HT system. The additional, important novelty of the work is a formula for tomographic transfer function for ISC-HT with conical illumination scenario.

The utility of the proposed algorithms was demonstrated by numerical simulations and an experimental measurement of a pancreatic tumor cell. The obtained results proved that the proposed space-domain algorithms prohibit the blurring effect, which is typical for DI. Moreover, it was proven that ISC-FBPP and DI suffer from the  $z$ -variant accuracy, which originates from the invalid use of the Rytov approximation. The experimental results showed that the  $z$ -variant accuracy is an important problem even for relatively small samples, such as a single biological cell, whose size in  $z$  direction is less than  $15\mu\text{m}$ . Moreover, the  $z$ -variant performance of DI and ISC-FBPP results in significant distortions, i.e. the reconstructions at nonzero  $|z|$  suffer from focusing-like deformation, which hinders evaluation of size and refractive index values of a specimen. This problem is overcome with ISC-EDOF-FBPP, which uses rigorous AS propagation instead of the approximated one, and therefore provides uniform accuracy in a large reconstruction volume. Notably, the price for the improved reconstruction accuracy of ISC-FBPP and ISC-EDOF-FBPP is increased computational load.

## Appendix

Holographic tomography with conical illumination scenario utilizes rotation of an inclined illumination direction around the optical ( $z$ ) axis. In the system, the inclination angle  $\alpha_{\text{ill}}$  of the illumination direction with respect to the  $z$  axis is fixed while the azimuth of illumination  $\theta$  is varied with a constant step in a full angle. Tomographic transfer function  $c$  of such a system can be represented as a sum of multiple spherical Ewald caps corresponding to successive illumination directions (Fig. 15(a)). Due to the symmetry of the illumination scenario, the function  $c$  is symmetric around the frequency axis  $K_z$ .

Let us first focus on the transverse cross-section of  $c$ , which contains the centers of curvature:  $S=[K_{Sx}, K_{Sy}, K_{Sz}]=[k_0n_0\sin\alpha_{\text{ill}}\cos\theta, k_0n_0\sin\alpha_{\text{ill}}\sin\theta, -k_0n_0\cos\alpha_{\text{ill}}]$  of the Ewald spheres (Fig. 15(b)). The function  $c$  is symmetric around  $K_z$ , thus, it is sufficient to find the values of  $c$  along a single transverse direction, e.g. along the  $K_y$  axis.

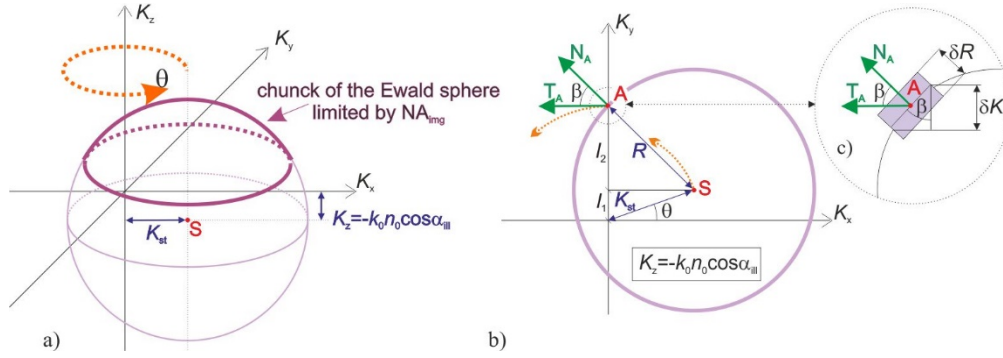


Fig. 15. The single Ewald sphere contribution: a) 3D view; b) cross-section at  $K_z = -k_0 n_0 \cos \alpha_{\text{ill}}$ .

The value of  $c$  at the frequency point A (Fig. 15(b)), which is located on the  $K_y$  axis, can be evaluated from the contribution of Ewald sphere with the inclination angle  $\theta$ . The corresponding coordinate  $K_{yA}$  is given by:

$$K_{yA} = l_1 + l_2 = K_{St} \sin \theta + \sqrt{R^2 - K_{St}^2 \cos^2 \theta}, \quad (14)$$

where  $R = k_0 n_0$  is a radius of curvature of the Ewald sphere and  $K_{St} = \sqrt{K_{Sx}^2 + K_{Sy}^2} = R \sin \alpha_{\text{ill}}$  denotes a transverse coordinate of the sphere centre. Contribution from the current Ewald sphere at the point A to the tomographic transfer function is proportional to  $1/\cos \beta_A$  [27], where  $\beta_A$  is an angle between directions  $T_A$  and  $N_A$ , where  $T_A$  indicates the direction of local translation of the cap with a change of  $\theta$  and  $N_A$  is a vector that is normal to the spherical surface at the point A. This is related to the fact that  $1/\cos \beta_A$  is proportional to volume of a chunk of the Ewald sphere of infinitesimal thickness  $\delta R$  at the point A (Fig. 15(c)):

$$V_A = \delta K_{yA} \cdot \delta k_{zA} \cdot \delta R / \cos \beta_A. \quad (15)$$

The value of  $\cos \beta_A$  in the function of  $K_{yA}$  can be found from Eq. (14) and:

$$\cos \beta_A = K_{St} \cos \theta / R, \quad (16)$$

giving:

$$\cos \beta_A = \sqrt{2(K_{yA}^2 R^2 + K_{yA}^2 K_{St}^2 + R^2 K_{St}^2) - K_{yA}^4 - K_{St}^4 - R^4} / 2K_{yA} R. \quad (17)$$

The distribution  $c$  is symmetric around the  $K_z$  axis. Therefore, replacing the coordinate  $K_{yA}$  in Eq. (17) with a transverse coordinate  $K_t = (K_x^2 + K_y^2)^{1/2}$  allows finding the contributions from all Ewald spheres and evaluate the tomographic transfer function  $c$ :

$$c(K_t, K_z = -k_0 n_0 \cos \alpha_{\text{ill}}) = \frac{2K_t R}{\sqrt{2(K_t^2 R^2 + K_t^2 K_{St}^2 + R^2 K_{St}^2) - K_t^4 - K_{St}^4 - R^4}} \cdot \frac{L}{2\pi K_t} \quad (18)$$

for the middle section, where  $L$  is a number of the applied illumination directions. Equation (18) can be generalized to other  $K_z$  slices, which leads to:

$$c = \frac{RL}{\pi \sqrt{2(K_t^2 R^2 + K_t^2 k_{St}^2 + R^2 K_{St}^2 + K_z^2 R^2 - K_t^2 K_z^2 - K_{St}^2 K_z^2) - K_t^4 - K_{St}^4 - R^4 - K_z^4}}, \quad (19)$$

where  $K'_z = K_z + R \cos \alpha_{\text{ill}}$ . Obviously,  $c$  is nonzero only in the region, which is occupied by the Ewald spheres:

$$\sqrt{R^2 - (K_t - K_{st})^2} - R \cos \alpha_{ill} > K_z > \sqrt{R^2 - (K_t + K_{st})^2} - R \cos \alpha_{ill}. \quad (20)$$

Lastly, in the real-life experimental setups, size of the Ewald caps is limited by a semi-aperture angle  $\alpha_{img}$  (Fig. 15(a)), which is related to numerical aperture  $NA_{img}$  of an imaging system:  $\alpha_{img} = \text{asin}(NA_{img}/n_0)$ . Therefore, the distribution  $c$  is zero for  $K'_z < R \cos \alpha_{img}$ . The result of the calculation of  $c$  for  $NA_{img}=1$  and  $\alpha_{ill}=60^\circ$  is presented in Fig. 7(d)-7(f).

### Funding

National Science Centre, Poland (2015/17/B/ST8/02220, 2015/19/N/ST7/03065, 2016/20/T/ST7/00330); Foundation for Polish Science (stipend START); Warsaw University of Technology (the Dean's grant 504/02222/1143/42.000000 and the statutory funds).

### Acknowledgments

The authors acknowledge the support of Lena Kastl (University of Muenster, Germany) for preparing the tumor cell sample and Ludwik Jaksztas (Warsaw University of Technology, Poland) for help in evaluating the tomographic transfer function.